Nanoscale

ROYAL SOCIETY OF CHEMISTRY

COMMUNICATION

View Article Online
View Journal | View Issue

Cite this: *Nanoscale*, 2025, **17**, 14125

Received 17th March 2025,
Accepted 16th May 2025

DOI: 10.1039/d5nr01116g

rsc.li/nanoscale

Ultra-uniform high-quality plasmonic metasurfaces through electrostatic self-assembly of gold nanoparticles on chemically unmodified glass†

Adriano Acunzo, [a,b] Maria De Luca, [a] Daniele Marra, [a] Bartolomeo Della Ventura, [a] Andreas Offenhäusser, [b] Dirk Mayer *[b] and Raffaele Velotta *[a]

We present a novel method for the fabrication of ultra-uniform metasurfaces through the direct electrostatic self-assembly of positively charged gold nanoparticles (AuNPs) on chemically unmodified glass. The method was successfully applied to two types of ultra-uniform AuNPs like nanospheres and nanocubes differing in shape, size, and cationic surfactant ligands, proving the versatility of the proposed methods. Unlike previous studies, we found that the AuNP clustering was due to improper drying of the metasurfaces after the deposition and not to instability of the colloids. Our fabrication methods resulted in metasurfaces of high densities and ultra-uniform arrangements with negligible clustering at both the microscale and macroscale, as confirmed by microscopic, spectroscopic, and nanophotonic analyses. Furthermore, thanks to far-field dipole couplings, the plasmon resonances of metasurfaces were significantly narrower (and blueshifted) compared to the corresponding colloid. Combined with the ultra-uniformity feature, these plasmon phenomena increased the quality factors (*Q*) of metasurfaces up to ~15. The densities, uniformities, and *Q*-factors of our metasurfaces are among the highest reported until now for similar nanostructures realized through the electrostatic self-assembly technique. Our findings demonstrate new possibilities to achieve higher *Q*-factors through simple, scalable, and cost-effective electrostatic self-assembly processes, with practical implications in optical sensing and nanophotonics. Moreover, the ultra-uniformity achieved by our methods opens up new opportunities to study the far-field dipole couplings in random arrays of anisotropic AuNPs.

Introduction

Nanofabrication science generally relies on two complementary approaches for the fabrication of plasmonic metasurfaces, named 'top-down' and 'bottom-up' methods.[1,2] Top-down methods, such as electron-beam and nanoimprint lithography, can define virtually any pattern with sub-10 nm resolution, but they require expensive clean-room facilities, high-vacuum or serial writing steps, and thus suffer from limited throughput and high costs. In contrast, bottom-up approaches, such as colloidal and block-copolymer micelle lithography, harness the spontaneous ordering of building blocks over wafer-scale areas in a single step, offering large-area coverage at low cost, albeit with larger feature sizes and more modest control over geometry. When the absolute performance is not the sole consideration, as in high-throughput sensing or integrated nanophotonics,[1,2] bottom-up methods can provide a superior quality–price trade-off. Among these latter methods, electrostatic self-assembly stands out as one of the simplest, most scalable, and most cost-effective techniques for assembling nanoparticles (NPs) into plasmonic metasurfaces, even though apparently it does not offer the best quality and performance of the class. A survey of the literature revealed that plasmonic metasurfaces are often realized through electrostatic self-assembly of negatively charged gold nanoparticles (AuNPs) on substrates like Si/SiO_2 or glass,[3–5] electrodes,[6] optrodes,[7] and many others. These substrates usually have negatively charged interfaces requiring chemical treatments to acquire the positive charge demanded by the deposition of negatively charged NPs. Chemical modifications are usually realized through the adsorption of cationic species like silanes,[8,9] organothiols,[4,9] and polyelectrolytes,[10,11] creating positively charged adhesive films atop the substrates. Intermediate films are adopted even when positively charged AuNPs are used.[12,13] In this case, a bottom cationic layer (*e.g.*, a silane or a cationic polyelectrolyte) is firstly adsorbed on the substrate, followed by the adsorption of a top anionic layer (*e.g.*, an anionic polyelectrolyte), allowing

[a]*Department of Physics "E. Pancini", University of Naples "Federico II", Via Cintia 26, 80126 Napoli, Italy. E-mail: rvelotta@unina.it*
[b]*Institute of Biological Information Processing (IBI-3), Bioelectronics, Forschungszentrum Jülich, 52425 Jülich, Germany. E-mail: dirk.mayer@fz-juelich.de*
† Electronic supplementary information (ESI) available. See DOI: https://doi.org/10.1039/d5nr01116g

for the binding of the positively charged AuNPs. It is understood that the main reason for functionalizing the substrates is to endow them with the high surface charge needed for the electrostatic deposition of oppositely charged AuNPs. However, the resulting adhesive films are often unstable. The charged molecules can indeed desorb, especially if the film is not a monolayer, causing detachment of NPs. Moreover, non-uniform adhesive films result in non-uniform surface charge, leading to non-uniform AuNP arrangements and, in particular, AuNP clustering.

A strategy to overcome these issues is the direct deposition of positively charged AuNPs onto negatively charged substrates without any chemical modification. Despite its potential, few studies have investigated this method. A recent series of works[14–16] demonstrated the electrostatic deposition of cysteamine-capped AuNPs on unmodified Si/SiO_2 substrates, with the surface density of AuNPs tuned by the ionic strength of the colloids. However, the resulting metasurfaces lacked uniformity, especially at high surface coverages, due to AuNP clustering induced by the high salt content of the colloid. Moreover, the cationic AuNPs resulted from a time-consuming post-synthesis modification of negatively charged AuNPs by the cationic cysteamine hydrochloride. It would be desirable to work with AuNPs naturally endowed with positive charges and avoid additives making the colloids unstable and hampering the uniformity of the metasurfaces. In this regard, Shao *et al.*[17] demonstrated the electrostatic deposition of positively charged cetyltrimethylammonium bromide (CTAB)-capped AuNPs onto some unmodified substrates like glass, mesoporous silica and titania films. A low CTAB concentration (~2 μM) was needed for a decent AuNP deposition, which was hindered at higher concentrations by competition with free cationic molecules. The method was successfully applied to AuNPs of varying shapes and sizes. However, even these metasurfaces lacked uniformity because of AuNP clustering ascribed to instabilities of the colloids at such low CTAB concentrations.

In this work, we hypothesized that the electrostatic self-assembly technique could allow the fabrication of ultra-uniform metasurfaces provided that specific conditions were satisfied: (1) NP monodispersion; (2) the use of chemically unmodified substrates; and (3) the use of appropriate drying methods. Therefore, we employed ultra-high yield synthesis methods, resulting in AuNPs naturally endowed with positive charges. These AuNPs were deposited onto pristine glass slides naturally endowed with negative charges under suitable conditions.[18,19] Finally, we developed a dedicated two-step drying procedure capable of minimizing the capillary forces among the freshly immobilized AuNPs,[20] the main source of clustering. Our refined methods resulted in metasurfaces of unprecedented density and uniformity for the electrostatic self-assembly technique. Moreover, thanks to far-field couplings,[21,22] the metasurfaces exhibited plasmon resonances significantly narrower (and blueshifted) compared to the starting colloids, resulting in quality factors (Q) among the highest reported until now for similar AuNP metasurfaces fabricated through the same technique.

Results and discussion

Ultra-uniform AuNSs and AuNCs

Ultra-uniform AuNPs were synthesized using seed-mediated growth methods[23–25] combined with Liz-Marzán's oxidative dissolution reaction.[26] In particular, we synthesized two types of positively charged NPs like CTAB-capped gold nanospheres (AuNSs) and cetylpyridinium chloride (CPC)-capped gold nanocubes (AuNCs) differing in shape, size, and ligand capping. Short and detailed descriptions of our optimized protocols can be found in the Methods section and in section 1.1 of the ESI,† respectively.

Fig. 1a and b display typical top-view and 52°-tilted STEM micrographs at high magnification of a typical batch of AuNSs, respectively. Quantitative analyses of shape and size were conducted on the top-view STEM micrograph in Fig. 2b to consider a sample of 550 NPs for higher statistics. All NPs had a spherical shape (shape yield ~100%) as confirmed by the aspect ratio (AR) and circularity (C) distributions of mean values $\overline{AR} = 1.05 \pm 0.03$ and $\bar{C} = 0.94 \pm 0.02$, respectively (see the ESI, section S1†). Furthermore, the sputtering-corrected diameter (D) distribution was well described by a Gaussian curve of mean $\bar{D} = 104 \pm 2$ nm (see the ESI, sections S1 and S2†). Therefore, the CTAB-capped AuNSs were spherical and monodisperse. Fig. 1c shows the normalized extinction spectrum of the as-synthesized AuNS colloid as a solid black line, exhibiting a localized surface plasmon resonance (LSPR) at 580 ± 1 nm with a full width at half maximum (FWHM) of 98 ± 1 nm. The dotted blue line refers to the finite-difference time-domain (FDTD) simulation of a single 104 nm gold sphere enclosed in a 3 nm thick CTAB shell and embedded in a saturated CTAB solution, mimicking the experimental conditions. This simulated spectrum (which refers to a single object) perfectly aligns to the experimental one (which refers to trillions of NPs) along the entire visible range, in particular, exhibiting the same LSPR and FWHM. This result theoretically confirmed the nearly perfect spherical shape and the monodispersion of the AuNS colloids.

Analogous characterization studies and analyses were conducted for a typical AuNC colloid. Fig. 1d and e display typical top-view and 52°-tilted STEM micrographs at high magnification of AuNCs, respectively, showing cubic or parallelepiped NPs characterized by flat {100} facets, rounded {110} edges and truncated {111} vertices.[27] Quantitative analysis of shape and size was conducted on a sample of 200 NPs from two top-view STEM micrographs of a typical AuNC metasurface (see the ESI, section S3†). Almost all NPs are cuboidal while other shapes are almost absent (shape yield > 95%). The AR (length : width) distribution had a mean value of $\overline{AR} = 1.12 \pm 0.10$, while the distribution of sputtering-corrected (and artifact-corrected) edges (E) was well fitted by a bi-Gaussian curve with a main peak at $\overline{E_1} = 74 \pm 5$ nm and a secondary minor tail at $\overline{E_2} = 92 \pm 7$ nm, the latter associated with a small population of overgrown edges (see the ESI, section S3†). Therefore, the vast majority of the AuNCs were either cubes or parallelepipeds slightly deviating from the cubic shape. Furthermore, the

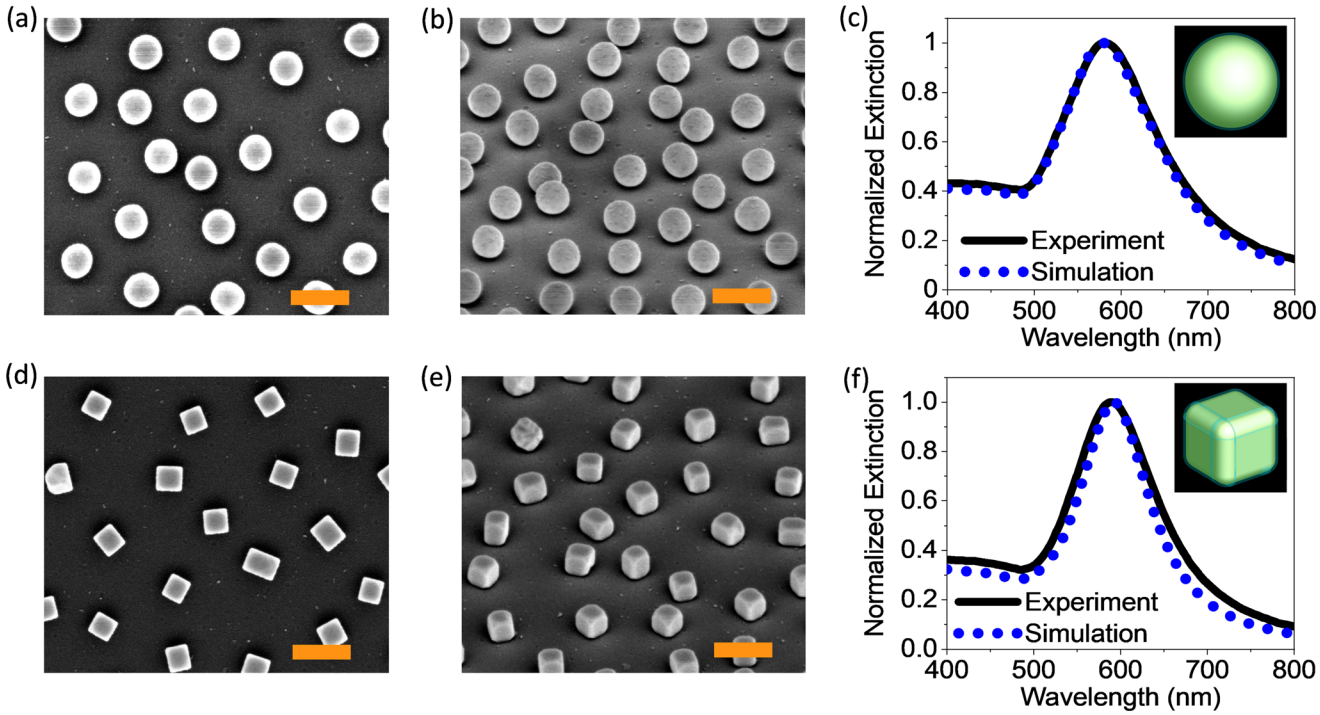

Fig. 1 Morphological and optical characterization of the AuNS and AuNC colloids. (a and d) Top-view and (b and e) 52°-tilted STEM micrographs at high magnification of the AuNSs and AuNCs, respectively. Scale bars: 200 nm. (c and f) Experimental (solid black) and simulated (dotted blue) normalized extinction spectra of the AuNS and AuNC colloids at 0.5 mM CTAB and 1 mM CPC, respectively. The insets are snapshots from the Lumerical workspace showing the NP models (enclosed in a dielectric shell) used for the FDTD simulations.

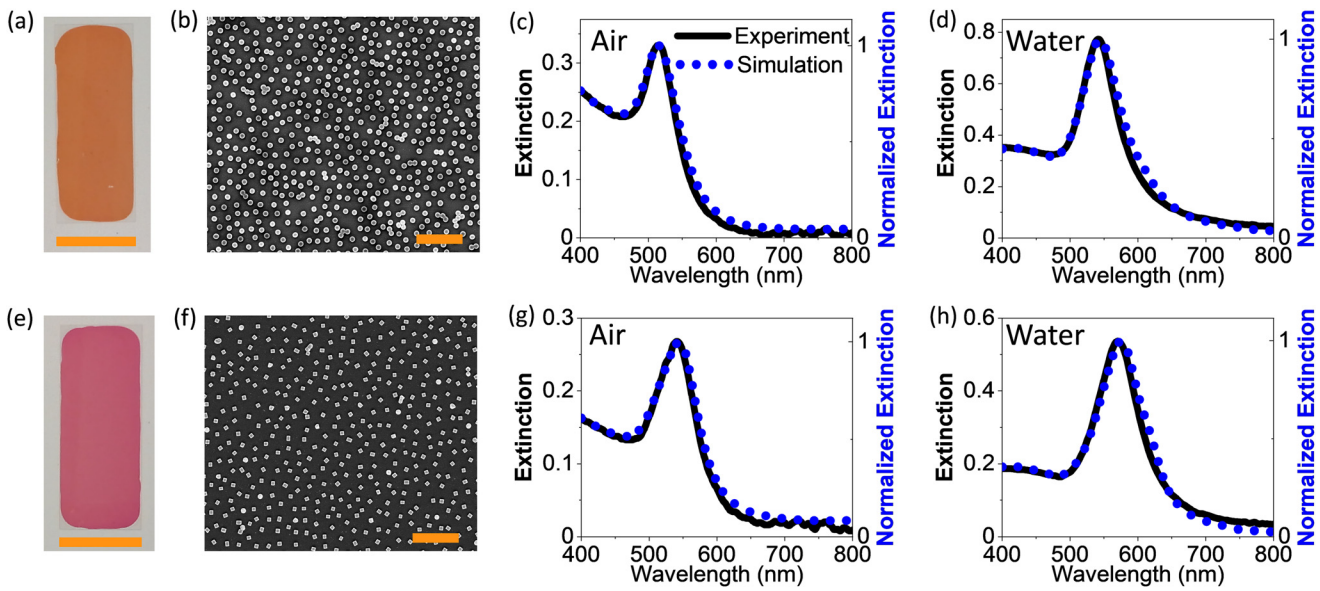

Fig. 2 Morphological and optical characterization of the metasurfaces. (a and e) Photographs of the AuNS and AuNC metasurfaces on chemically unmodified glass coverslips, respectively. Scale bars: 24 mm. (b and f) Typical top-view STEM micrographs of the AuNS and AuNC metasurfaces, respectively. Scale bars: 1 μm. (c and g) Experimental (solid black) and simulated (dotted blue) extinction spectra of the AuNS and AuNC metasurfaces in air, respectively. (d and h) Corresponding spectra in water medium.

mean radius of curvature $\overline{R_{curv}}$ of the AuNC corners was estimated as $\overline{R_{curv}} = 12 \pm 2$ nm by considering the 68 visible corners of the AuNCs visible in Fig. 1d. The complete analysis is detailed in the ESI, section S4.† Finally, Fig. 1f shows the normalized experimental extinction spectrum of the as-synthesized AuNC colloid as a solid black line, exhibiting a LSPR

peaked at 590 ± 1 nm with a FWHM of 91 ± 1 nm. For the simulations, the "all rounded quadrilateral" from Lumerical's object library—a parallelepiped with edges and corners rounded by cylinders and spheres, respectively—was chosen as accurately reproducing the crystallographic features of the real AuNCs. A 3 nm-thick dielectric shell and an embedding medium replicating the experimental conditions were also considered for these simulations. The best model was obtained by fixing the edges to the experimental mean value $\overline{E_1}$ while optimizing the R_{curv} against the experimental spectrum. This optimization yielded an optimal value of R_{curv} = 14 nm, consistent with the morphological analysis. The dotted blue line in Fig. 1f refers to the simulated spectrum of this optimal model. It exhibits a LSPR peaked at 592 ± 1 nm with a FWHM of 78 ± 1 nm, which is ~14% narrower than the experimental one. This discrepancy obviously reflects the slight polydispersion of the colloids, whereas the simulation referred to a single object representing the average AuNC. It is worth noting that the polydispersion could be further reduced by an iterative synthesis technique.[23] However, we were already satisfied with the result and preferred a shorter protocol to save time.

It is also worth stressing that the seed-mediated growth methods[23–25] used to synthesize our AuNPs yielded highly reproducible results. In fact, the amount of seeds added to the (fixed) growth solutions can be easily adjusted for each new synthesis to obtain the desired result. This high reproducibility is reflected in the statistical data over multiple samples provided in Table 1.

In light of the aforementioned experimental and simulation results, the first prerequisite for ultra-uniform metasurfaces, *i.e.*, the ultra-uniformity of NPs, was considered satisfied.

Ultra-uniform metasurfaces

Among the substrates that are naturally endowed with a negative surface charge, borosilicate glass seemed to us the obvious choice. In fact, borosilicate glass has a high SiO_2 content (~65%) that makes its interfaces similar to Si/SiO_2 interfaces. The latter are naturally rich in silanol bonds which ensure negative surface charges when in contact with electrolyte solutions of pH $\gtrsim$ 4.[18] As the electrolyte pH increases, the interface becomes more negatively charged.[18] Moreover, the charge can be further increased and made more uniform by fully oxidizing the interface by a simple oxygen plasma treatment, so-called "activation". An activated Si/SiO_2 interface can exhibit a ζ-potential as high as −70 mV at neutral pH.[18] Glass was thus expected to have similar features. Given the role of the electrolyte, we measured the pH of our AuNP colloids at an optical density (OD) of OD = 5 (used for deposition) and surfactant bulk concentrations ranging from 1 μM to 10 mM. To keep these concentrations under strict control, the as-synthesized colloids (AuNSs at 0.5 mM CTAB and AuNCs at 1 mM CPC) were subjected to 2–3 rounds of centrifugation, each time resuspending the pellets with the respective surfactant solutions at the desired concentration. The results were similar for both colloids and essentially equal to the pH values of the surfactants themselves:[28] pH ~5.4 for colloids at $\gtrsim$100 μM CTAB/CPC; pH ~7.4 for colloids at $\lesssim$1 μM CTAB/CPC; and a logarithmic scale in the range of ~1–100 μM. These pH values alone would suggest that AuNP deposition onto activated glass would be possible even for colloids at high surfactant concentrations. However, it is well known that surfactants like CTAB stick to silica surfaces, implying a surface charge reversal at ~10–60 μM.[29] In fact, we observed deposition only for colloids at $\lesssim$1 μM CTAB/CPC, clearly indicating that competition between the free surfactant cations and the surfactant-capped AuNPs prevented the electrostatic binding of the latter at surfactant concentrations of $\gtrsim$1 μM because of the above-mentioned effect.

It is worth noting that the instability threshold for the CTAB-capped AuNP colloids was estimated as ~2 μM in a previous study.[17] This conclusion was based on evidence of AuNP clusters in metasurfaces fabricated through the electrostatic self-assembly deposition of CTAB-capped AuNP colloids at that specific CTAB concentration. Unlike this conclusion, we found our colloids to be stable at this surfactant concentration, while becoming unstable at ~0.25 μM CTAB/CPC. Instead, we found that clustering occurred because of the drying steps. In particular, we observed irreversible changes of the color of fresh metasurfaces when taking them out of the ultrapure water bath used for post-deposition washing steps (see the ESI, section S5†). We ascribed the phenomenon, systematically occurring at the water/air interface, to excessive capillary forces among the AuNPs due to the high surface tension of ultrapure water. The issue was overcome by introducing a solvent exchange step right before the drying of the metasurfaces. Specifically, at step 5 of our fabrication protocol (see the ESI, section 1.2†), ultrapure water was slowly replaced by dropwise adding a 5% isopropyl alcohol (IPA) aqueous solution to the

Table 1 Summary of key parameters for the AuNP colloids and metasurfaces of this work. For each parameter, the mean and its standard deviation were calculated for a set of four samples

	Size (nm)	LSPR (nm)	FWHM (nm)	*Q*-Factor	σ (NPs per μm^2)	NND (nm)	% clusters
AuNS colloids	104 ± 1	580 ± 1	98 ± 1	5.9 ± 0.1	n/a	n/a	~0
AuNS metasurfaces in water	104 ± 1	542 ± 1	48 ± 1	11.3 ± 0.2	19 ± 1	188 ± 5	4 ± 1
AuNS metasurfaces in air	104 ± 1	515 ± 1	34 ± 1	15.1 ± 0.4	19 ± 1	188 ± 5	4 ± 1
AuNC colloids	75 ± 1	590 ± 1	91 ± 1	6.5 ± 0.1	n/a	n/a	~0
AuNS metasurfaces in water	75 ± 1	571 ± 1	61 ± 1	9.4 ± 0.2	14 ± 1	226 ± 4	2 ± 1
AuNS metasurfaces in air	75 ± 1	541 ± 1	49 ± 1	11.0 ± 0.2	14 ± 1	226 ± 4	2 ± 1

ultrapure water bath just used for the post-deposition washing step. The new liquid avoided the aforementioned phenomenon. In particular, a thin layer of IPA solution wetted the metasurfaces even after their removal from the Petri dish, allowing controlled drying under a vigorous stream of nitrogen. The aforementioned procedure worked equally well when employing a 5% ethyl alcohol (EtOH) aqueous solution, owing to the similar physicochemical properties of EtOH and IPA. In contrast, the procedure failed when using pure or concentrated IPA or EtOH aqueous solution (*e.g.*, 50% IPA or EtOH), as the AuNPs detached from the glass substrate during either the solvent exchange or the drying step. This behavior was attributed to the higher solubility of CTAB and CPC surfactant molecules in concentrated IPA and EtOH solutions compared to dilute solutions or water, which likely facilitated their desorption from the surfaces of the surfactant-capped AuNPs previously immobilized on the substrate. The resulting reduction in the positive surface charge of AuNPs, conferred by the surfactant capping layer, may readily account for their detachment under these different solvent conditions. Our fabrication procedure also prescribed a final low-pressure oxygen plasma treatment to remove organic trace residues (*e.g.*, surfactant residues) from the metasurfaces. Besides the cleaning function, this treatment also served to increase the binding strength between the AuNPs and the glass substrate, as demonstrated in the literature.[18,19] Morphological alterations were no longer an issue after such treatment. For instance, no measurable changes in the metasurface extinction spectra were observed after overnight incubation in ultrapure water, PBS 1× and PBS 10×. It was only after tens of rinsing/drying cycles that minor changes in the spectra occurred, indicating a high stability of the plasma-treated metasurfaces. Eventually, the metasurfaces showed no measurable spectral changes for over 1 year when stored under standard conditions.

Short and detailed descriptions of the fabrication protocol are reported in the Methods section and in section 1.2 of the ESI,† respectively. It is worth stressing that such protocols refer to the most dense and uniform metasurfaces that could possibly be achieved. The following results refer to this case, the most interesting for this work. First, the uniformity and density of the as-fabricated AuNS and AuNC metasurfaces could be observed by the naked eye. Fig. 2a and e show photographs of typical AuNS and AuNC metasurfaces, respectively, both displaying brilliant and uniform colors all over the 24 × 60 mm glass coverslips. Typical STEM micrographs at low magnification are shown in Fig. 2b and f, respectively. They show NPs randomly distributed over large areas ($\gtrsim$30 μm^2) as individual particles and minimal clustering. Specifically, the fraction of clusters is $\lesssim$5% in the case of the AuNS metasurfaces (528 visible structures, of which 505 are single AuNSs and 23 are clusters counting 65 AuNSs organized as dimers or trimers), and ∼2% in the case of the AuNC metasurfaces (398 visible structures, of which 390 are single AuNCs and 8 are clusters counting 18 AuNCs organized as dimers, trimers, or occasionally stacked AuNCs). Quantitative analysis of the nearest-neighbor center-to-center distance (NND) distribution of the AuNPs showed visual evidence of high uniformity (see the ESI, section S6†). For the AuNS metasurfaces, excluding the first two bins counting the AuNSs organized as clusters, the Gaussian fit yielded a mean $\overline{\mathrm{NND}} = 192 \pm 22$ nm, while for the AuNC metasurface it yielded $\overline{\mathrm{NND}} = 223 \pm 33$ nm, *i.e.*, they are both characterized by relatively small standard deviations. Furthermore, the NND distributions are obviously related to the surface densities of AuNSs and AuNCs. In the case of AuNS metasurfaces, the mean interparticle gap (g) is $88\ \mathrm{nm} = g < \bar{D}$, indicating that there is usually insufficient space for an additional AuNS to be positioned in between two neighboring AuNSs. Therefore, this NND distribution reflects a relatively high surface density, estimated as $\sigma \approx 19$ AuNSs per μm^2. In this regard, it is noteworthy that small areas (∼1 μm^2) of the AuNS metasurfaces (see Fig. 2b) occasionally exhibit a quasi-hexagonal arrangement, *i.e.*, the maximum packing configuration for spheres. Instead, for the AuNC metasurfaces, there is typically enough space for another AuNC to be placed in between two neighboring AuNCs, being $149\ \mathrm{nm} = g > \overline{E_1}$. This NND distribution reflects a relatively lower surface of density $\sigma \approx 14$ AuNCs per μm^2. We ascribed this lower surface density to different AuNC/glass and AuNC/AuNC interactions compared to the case of AuNSs, likely due to the different surfactants. However, the uniformity and density of both metasurfaces are among the highest found in the literature for similar AuNP nanostructures fabricated through electrostatic self-assembly and other nanolithography techniques.[17,21,30,31]

The metasurfaces were also optically characterized through UV-vis extinction spectroscopy when placed in two different media such as air and ultrapure water (see the Methods section). Typical spectra are shown as solid black lines in Fig. 2c and d for AuNS metasurfaces in air and water, respectively, and in Fig. 2g and h for AuNC metasurfaces in air and water, respectively. The AuNS metasurfaces typically exhibited a LSPR peaking at 515 ± 1 nm with a FWHM of 34 ± 1 nm and an OD of ∼0.33 in air, and a LSPR peaking at 542 ± 1 nm with a FWHM of 48 ± 1 nm and an OD of ∼0.77 in ultrapure water. Similarly, the AuNC metasurfaces exhibited a LSPR peaking at 541 ± 1 nm with a FWHM of 49 ± 1 nm and an ODof ∼0.27 in air; and a LSPR peaking at 571 ± 1 nm with a FWHM of 61 ± 1 nm and an OD of ∼0.54 in ultrapure water. No secondary LSPRs or shoulders at longer wavelengths were observed, indicating minimal clustering also at the macroscopic scale. It is worth mentioning that the relatively high ODs of our metasurfaces corresponded to one NP monolayer, and not two monolayers, one on the top and one on the bottom substrate surfaces, as often reported in the literature.[17,30,32] This practical feature was inherent in our deposition method (see the ESI, section 1.2†). The dotted blue lines in Fig. 2c and d and 2g and h refer to the FDTD simulations of faithful models of the STEM micrographs in Fig. 1a and d, respectively. Full details about the processing and modelling of the micrographs are reported in the ESI, section S7,† for the most complex case of the AuNC metasurfaces. Technical details about the simulations can be found in the Methods section. Notably, each simulated spectrum perfectly aligned with the corresponding

experimental spectrum. Since the simulations considered local geometries (the micrographs cover a microscopic area of ~1 μm^2), whereas the experimental spectra refer to macroscopic regions of the metasurfaces (the area intercepted by the spectrophotometer light beam is a few mm^2), the aforementioned agreement between the experimental and simulated spectra theoretically confirmed the uniformity of our metasurfaces at the macroscale.

It is also worth emphasizing that minimal variations were observed across multiple samples, see Table 1. This high reproducibility was a direct consequence of the minimization of clustering ensured by our fabrication method, as well as the ultra-uniformity and reproducibility of the AuNPs themselves.

The results shown in this section conclusively demonstrate the ultra-uniformity of our AuNS and AuNC metasurfaces at the macroscale. To the best of our knowledge, these arrays are among the most uniform and dense metasurfaces fabricated until now through the electrostatic self-assembly technique.

High-quality metasurfaces

An obvious observation about the metasurfaces is that their LSPRs were significantly blueshifted and narrower than the corresponding colloids, see Fig. 3a and b. These peculiar plasmon phenomena are due to far-field dipole couplings among relatively big nanoparticles,[21,22] which decrease the real and imaginary parts of the retarded dipole sum of the particle ensemble compared to the single-particle case, yielding the LSPR blueshift and narrowing, respectively.[33,34] Some aspects of these phenomena, *e.g.*, whether the blueshift is due to changes in the absorption or scattering contributions of the nanoparticle ensemble, are still missing[31] and will be the object of a future study. Here, we stress that the quality factor $Q \equiv$ LSPR/FWHM of our metasurfaces significantly increased as a consequence of the aforementioned effects and their ultra-uniformity. In fact, minimal NP clustering implies minimal near-field coupling, which is generally associated with a broadening of the LSPR which, in turn, would compete with the narrowing effect of far-field coupling. In particular, in the case of AuNSs, the Q-factor changed from $Q \approx 6$ of the colloid to $Q \approx 11$ of the metasurface in water to $Q \approx 15$ of the metasurface in air. Analogously, in the case of AuNCs, the Q-factor changed from $Q \approx 6.5$ of the colloid to $Q \approx 9.5$ of the metasurface in water to $Q \approx 11$ of the metasurface in air. These Q-factors are among the highest reported so far using similar metasurfaces fabricated through the electrostatic self-assembly technique. In fact, they are even comparable with the Q-factors of surface lattice resonances[1] (SLRs) measured for hexagonally ordered AuNP metasurfaces fabricated through more sophisticated lithography techniques.[31,35]

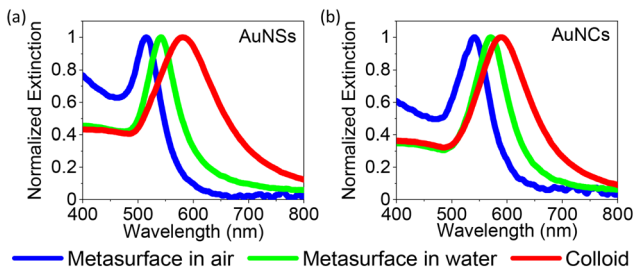

Fig. 3 Comparison between the experimental spectra of the metasurfaces in air and water media and their corresponding colloids. (a) AuNSs. (b) AuNCs. Thanks to long-range dipole couplings, the LSPRs of metasurfaces were blueshifted and narrower than the corresponding colloids, thus resulting in higher Q-factor resonances.

Conclusions

We have shown that the electrostatic self-assembly technique results in ultra-uniform AuNP metasurfaces whenever certain conditions are satisfied. In particular, we found the main obstacle to be in the post-deposition step of drying, which is generally associated with excessive capillary forces inducing the clustering of freshly deposited AuNPs. In combination with monodisperse AuNPs and a chemically unmodified glass substrate, a refined drying procedure addressed the issues and resulted in metasurfaces of unprecedented density and uniformity for the technique used. It is worth stressing that the same methods were indiscriminately applied to both CTAB- and CPC-capped AuNPs, obtaining comparable results. This was likely due to the similar chemical compositions and structures of CTAB and CPC. Considering that almost any kind of AuNP can be synthesized with these surfactants as native ligand capping agents, the fabrication methods introduced in this work could be straightforwardly extended to AuNPs of any shape and size, also potentially providing ultra-uniform metasurfaces. Moreover, the plasmon resonances exhibited by the fabricated metasurfaces were unexpectedly found to be blueshifted and, more importantly, narrower than those of the starting colloids. This effect, due to far-field dipole couplings, significantly increased the Q-factor of the metasurface resonances compared to the colloid, up to ~15. These Q-factors are among the highest reported so far for metasurfaces realized through the electrostatic self-assembly technique. While our method could not achieve either the sub-10 nm precision and order of top-down nanolithography techniques or the resulting ultrahigh SLR Q-factors (10^2–10^3), it represents a smart route for enhancing Q-factors through a much simpler, scalable, and cost-effective self-assembly process. In fact, our approach operates under ambient conditions, requires no clean-room facilities, uses inexpensive chemicals and substrates, and routinely yields macroscopic samples (≥10 cm^2) with ultra-high uniformity and high Q-factors. These features significantly simplify fabrication, minimize batch-to-batch variations, reduce spectral noise, and increase refractive index sensitivity, paving the way for the development of low-cost, high-quality, and high-throughput biosensing platforms. Moreover, the ultra-uniformity achieved by our methods opens up new opportunities to study the far-field dipole couplings in random arrays of anisotropic AuNPs.

Materials and methods

Chemicals and solid substrates

All chemical reagents used for the synthesis of gold nanoparticles (AuNPs), including cetyltrimethylammonium bromide (CTAB, $C_{19}H_{42}BrN$), tetrachloroauric(III) acid trihydrate ($HAuCl_4{\cdot}3H_2O$), sodium borohydride ($NaBH_4$), silver nitrate ($AgNO_3$), L-ascorbic acid ($C_6H_8O_6$), cetylpyridinium chloride (CPC, $C_{21}H_{38}ClN$) and potassium bromide (KBr), were purchased from Sigma-Aldrich. These compounds were trace metal grade and used without further purification. Aqueous solutions of these compounds were prepared using ultrapure water (18.2 MΩ cm at 25 °C, 1.7 ppb TOC) from a Millipore Milli-Q IQ 7000 system. The substrates used for the fabrication of AuNP arrays were Menzel-Gläser glass coverslips (D263M colorless borosilicate glass) of standard sizes, 24 × 60 mm or 24 × 32 mm, and thickness no. 1 (0.13–0.16 mm), purchased from Thermo Fisher Scientific. Before use, they were sequentially cleaned with isopropyl alcohol (IPA) and ultrapure water in an ultrasonic bath for 5 minutes and finally dried under a gentle stream of nitrogen.

Synthesis of AuNPs

Gold nanosphere (AuNS) and gold nanocube (AuNC) colloids were synthesized by combining seed-mediated growth methods[23–25] with Liz-Marzán's dissolution reaction.[26] Our optimized protocols are detailed in the ESI,†, section 1.1. Briefly, CTAB-capped gold seeds (size:[24] <4 nm) were synthesized and grown into CTAB-capped gold nanorods (AuNRs), whose dissolution provided CPC-capped spherical gold seeds (size:[23] ∼20 nm). These latter were grown either into CPC-capped AuNCs or into CPC-capped gold concave rhombic dodecahedra (AuCRD). Dissolution of AuCRD resulted in CTAB-capped AuNSs.

Fabrication of ultra-uniform AuNP metasurfaces

AuNS and AuNC metasurfaces were obtained on chemically unmodified glass coverslips through the electrostatic self-assembly of the corresponding colloids. The full procedure is detailed in the ESI,† section 1.2, and refers to the most dense and uniform metasurfaces that could possibly be fabricated. Briefly, the as-synthesized CTAB-capped AuNS and CPC-capped AuNC colloids were brought to OD 5 and ∼0.5 μM CTAB and CPC through at least three rounds of centrifugations and resuspensions using 0.5 μM CTAB and CPC aqueous solutions, respectively. These colloids were pipetted onto the top surfaces of oxygen plasma activated glass coverslips (plasma parameters: 0.8 mbar, 200 W, 5 min) and allowed to stand for 4 h for deposition in a Petri dish. During this time, the positively charged AuNPs (due to the capping of cationic surfactants) electrostatically adsorbed onto the negatively charged glass surface (due to the plasma activation and pH conditions). Afterwards, the substrates were rinsed with ultrapure water to remove the unbound AuNPs. Then, the ultrapure water was slowly exchanged by dropwise adding a 5% IPA solution in a Petri dish. Finally, the samples were dried under a vigorous stream of nitrogen and cleaned from organic trace residues by a low-pressure oxygen plasma treatment (0.8 mbar, 200 W, 30 min and 0.8 mbar, 200 W, and 3 min for the AuNS and AuNC metasurfaces, respectively).

Characterization of AuNP colloids and metasurfaces

The UV-vis extinction spectra of colloids and metasurfaces were recorded using a DeNovix DS-11FX+ spectrophotometer. The spectra of the AuNP colloids were recorded in 10 mm path cuvettes. CTAB or CPC aqueous solutions at concentrations equal to the bulk CTAB or CPC concentrations of the investigated colloids served as reference samples for the 'blank' spectra. The spectra of the metasurfaces were also recorded in 10 mm path cuvettes. In this case, 10 mm width slices of the metasurfaces were cut using a diamond tip and placed in the cuvettes. The spectra of the metasurfaces in water medium were recorded after filling the cuvettes with ultrapure water. 10 mm width slices of pristine glass coverslips (placed in cuvettes possibly filled with ultrapure water) served as reference samples for the 'blank' spectra.

Top-view and 52°-tilted scanning transmission electron microscopy (STEM) micrographs of the AuNP metasurfaces were obtained using a FEI Magellan STEM microscope at the Helmholtz Nano Facility (HNF). All samples were imaged after iridium sputtering (60 s, 25 mA). The iridium sputtering layer had a nominal thickness of 6 nm, which was confirmed experimentally by a focused ion beam (FIB) cut of a metasurface sample performed using the FEI Helios FIB of the HNF, see the ESI section S2.† The thickness of the iridium sputtering layer was considered for the correct estimation of the AuNP dimensions. All STEM micrographs were analyzed using ImageJ Fiji software.

FDTD simulations

Finite-difference time-domain (FDTD) simulations were performed using Ansys Lumerical commercial software. Single-particle simulations were performed using the so-called "Mie scattering setup", whose detailed description can be found in previous works.[36,37] AuNSs were modelled as spheres while AuNCs were modelled as "all-rounded quadrilaterals", a built-in object consisting of a parallelepiped with edges and corners rounded by cylinders and spheres, respectively. Olmon's dataset[38] was chosen to reproduce the monocrystalline nature of both AuNPs. A 3 nm-thick dielectric shell of refractive index (RI) n = 1.4350 was used to reproduce the well-known CTAB[39–41] or CPC[42] bilayer capping. Finally, a background medium of RI n = 1.3478 was used to reproduce the experimental conditions of saturated CTAB or CPC aqueous solutions.[43] It is worth noting that these values strictly refer to CTAB, but were also assumed for CPC since reliable values for CPC were not found in the literature. The assumption was based on the chemical and structural similarities between the CPC and CTAB molecules. A 0.5 nm mesh override was used for NPs for high accuracy. Many-particle simulations (*i.e.*, concerning the metasurfaces) were performed using a standard setup for extended objects, consisting of a plane wave source, a

transmission plane monitor, and scatterers. The scatterers were accurate reproductions of the STEM micrographs in Fig. 1a and d, *i.e.*, AuNPs on a seemingly infinite glass slab of RI = 1.52. In order to reproduce the extended nature of the metasurfaces, periodic boundary conditions (rather than perfect matched layer boundaries) were set along the x and y axes of the simulation workspace. Consequently, the objects that were actually simulated were periodic arrays having as unit cells (models of) the STEM micrographs in Fig. 1a and d. No dielectric shells were added to the AuNPs this time, as the metasurfaces were cleaned of organic materials by a low-pressure oxygen plasma treatment. A 1.5 nm mesh override was applied to each scatterer compatibly with our computational resources.

Author contributions

AA: conceptualization, methodology, investigation, data curation, validation, formal analysis, software, visualization, and writing – original draft. MDL: formal analysis, software, visualization, and writing – review & editing. DM: visualization and writing – review & editing. BDV: conceptualization and writing – review & editing. AO: resources and funding acquisition. DM: conceptualization, supervision, data curation, project administration, and writing – review & editing. RV: conceptualization, supervision, project administration, writing – review & editing, and funding acquisition.

Data availability

The data supporting this article have been included as part of the ESI.†

Conflicts of interest

There are no conflicts to declare.

Acknowledgements

This project was partially funded by the Italian Ministry of University and Research (MUR) under the following grants: Ph. D. grant DOT 1318991-1 and PRIN project P2022J3ZPW. Additional funding was also provided by the European Union – Next Generation EU, Mission 4 Component 2 CUP 63C24001310005.

References

1 A. Minopoli, A. Acunzo, B. Della Ventura and R. Velotta, *Adv. Mater. Interfaces*, 2022, **9**, 2101133.
2 A. Acunzo, E. Scardapane, M. De Luca, D. Marra, R. Velotta and A. Minopoli, *Chemosensors*, 2022, **10**, 136.
3 T. Bartschmid, A. Farhadi, M. E. Musso, E. S. A. Goerlitzer, N. Vogel and G. R. Bourret, *ACS Appl. Nano Mater.*, 2022, **5**, 11839–11851.
4 M. Ben Haddada, M. Huebner, S. Casale, D. Knopp, R. Niessner, M. Salmain and S. Boujday, *J. Phys. Chem. C*, 2016, **120**, 29302–29311.
5 K. Winkler, M. Paszewski, T. Kalwarczyk, E. Kalwarczyk, T. Wojciechowski, E. Gorecka, D. Pociecha, R. Holyst and M. Fialkowski, *J. Phys. Chem. C*, 2011, **115**, 19096–19103.
6 G. Siciliano, A. Alsadig, M. S. Chiriacò, A. Turco, A. Foscarini, F. Ferrara, G. Gigli and E. Primiceri, *Talanta*, 2024, **268**, 125280.
7 F. Galeotti, M. Pisco and A. Cusano, *Nanoscale*, 2018, **10**, 22673–22700.
8 N. Aissaoui, L. Bergaoui, J. Landoulsi, J. F. Lambert and S. Boujday, *Langmuir*, 2012, **28**, 656–665.
9 L. Wang, U. S. Schubert and S. Hoeppener, *Chem. Soc. Rev.*, 2021, **50**, 6507–6540.
10 Y. C. Kim, S. Hoang, K. I. Winey and R. J. Composto, *ACS Appl. Mater. Interfaces*, 2024, **16**, 61083–61095.
11 S. M. Budy, D. J. Hamilton, Y. Cai, M. K. Knowles and S. M. Reed, *J. Colloid Interface Sci.*, 2017, **487**, 336–347.
12 M. V. Gutiérrez and A. F. Scarpettini, *Colloid Interface Sci. Commun.*, 2019, **33**, 100213.
13 T. Yang, D. Wang and X. Liu, *Colloids Surf., B*, 2019, **173**, 833–841.
14 M. Oćwieja, J. Maciejewska-Prończuk, Z. Adamczyk and M. Roman, *J. Colloid Interface Sci.*, 2017, **501**, 192–201.
15 M. Morga, M. Nattich-Rak, M. Oćwieja and Z. Adamczyk, *Phys. Chem. Chem. Phys.*, 2019, **21**, 6535–6543.
16 J. Maciejewska-Prończuk, M. Oćwieja, Z. Adamczyk and A. Pomorska, *Colloids Surf., A*, 2019, **560**, 393–401.
17 L. Shao, Q. Ruan, R. Jiang and J. Wang, *Small*, 2014, **10**, 802–811.
18 K. Greben, P. Li, D. Mayer, A. Offenhäusser and R. Wördenweber, *J. Phys. Chem. B*, 2015, **119**, 5988–5994.
19 A. Q. Tran, C. Kaulen, U. Simon, A. Offenhäusser and D. Mayer, *Biomater. Sci.*, 2017, **5**, 1051–1060.
20 T. Ghosh, E.-C. Fritz, D. Balakrishnan, Z. Zhang, N. Vrancken, U. Anand, H. Zhang, N. D. Loh, X. Xu, F. Holsteyns, C. A. Nijhuis and U. Mirsaidov, *ACS Appl. Mater. Interfaces*, 2022, **14**, 5537–5544.
21 J. A. Jenkins, Y. Zhou, S. Thota, X. Tian, X. Zhao, S. Zou and J. Zhao, *J. Phys. Chem. C*, 2014, **118**, 26276–26283.
22 F. Zhao, M. M. P. Arnob, O. Zenasni, J. Li and W.-C. Shih, *Nanoscale Horiz.*, 2017, **2**, 267–276.
23 M. N. O'Brien, M. R. Jones, K. A. Brown and C. A. Mirkin, *J. Am. Chem. Soc.*, 2014, **136**, 7603–7606.
24 B. Nikoobakht and M. A. El-Sayed, *Chem. Mater.*, 2003, **15**, 1957–1962.
25 W. Niu, S. Zheng, D. Wang, X. Liu, H. Li, S. Han, J. Chen, Z. Tang and G. Xu, *J. Am. Chem. Soc.*, 2009, **131**, 697–703.
26 J. Rodríguez-Fernández, J. Pérez-Juste, P. Mulvaney and L. M. Liz-Marzán, *J. Phys. Chem. B*, 2005, **109**, 14257–14261.
27 C.-J. Huang, P.-H. Chiu, Y.-H. Wang, W. R. Chen and T. H. Meen, *J. Electrochem. Soc.*, 2006, **153**, D129.

28 Y. Liu, M. Tourbin, S. Lachaize and P. Guiraud, *Chemosphere*, 2013, **92**, 681–687.
29 E. Tyrode, M. W. Rutland and C. D. Bain, *J. Am. Chem. Soc.*, 2008, **130**, 17434–17445.
30 D. Sun, F. Ben Romdhane, A. Wilson, M. Salmain and S. Boujday, *ACS Appl. Nano Mater.*, 2024, **7**, 5093–5102.
31 E. Ponomareva, K. Volk, P. Mulvaney and M. Karg, *Langmuir*, 2020, **36**, 13601–13612.
32 S. Y. Oh, N. S. Heo, V. K. Bajpai, S.-C. Jang, G. Ok, Y. Cho and Y. S. Huh, *Front. Bioeng. Biotechnol.*, 2019, **7**, 1–11.
33 D. Dey and G. C. Schatz, *MRS Bull.*, 2024, **49**, 421–430.
34 L. Zhao, K. L. Kelly and G. C. Schatz, *J. Phys. Chem. B*, 2003, **107**, 7343–7350.
35 K. Volk, J. P. S. Fitzgerald, P. Ruckdeschel, M. Retsch, T. A. F. König and M. Karg, *Adv. Opt. Mater.*, 2017, **5**, 1600971.
36 R. Campanile, A. Acunzo, E. Scardapane, A. Minopoli, V. C. Martins, R. Di Girolamo, S. Cardoso, R. Velotta, B. Della Ventura and V. Iannotti, *ACS Omega*, 2022, **7**, 36543–36550.
37 A. Minopoli, E. Scardapane, A. Acunzo, R. Campanile, B. Della Ventura and R. Velotta, *AIP Adv.*, 2021, **11**, 065319.
38 R. L. Olmon, B. Slovick, T. W. Johnson, D. Shelton, S.-H. Oh, G. D. Boreman and M. B. Raschke, *Phys. Rev. B: Condens. Matter Mater. Phys.*, 2012, **86**, 235147.
39 P. Kékicheff and O. Spalla, *Langmuir*, 1994, **10**, 1584–1591.
40 G. Szabó, E. Albert, J. Both, L. Kócs, G. Sáfrán, A. Szöke, Z. Hórvölgyi and L. M. Mureşan, *Surf. Interfaces*, 2019, **15**, 216–223.
41 S. Gómez-Graña, F. Hubert, F. Testard, A. Guerrero-Martínez, I. Grillo, L. M. Liz-Marzán and O. Spalla, *Langmuir*, 2012, **28**, 1453–1459.
42 A. Meleshyn, *Langmuir*, 2009, **25**, 881–890.
43 J. Cieśla, M. Koczańska, J. Narkiewicz-Michałek, M. Szymula and A. Bieganowski, *J. Mol. Liq.*, 2016, **222**, 463–470.